Materials Advances

ROYAL SOCIETY OF CHEMISTRY

PAPER

View Article Online
View Journal | View Issue

Cite this: *Mater. Adv.*, 2022, 3, 3642

Birefringence in anodic aluminum oxide: an optical method for measuring porosity†

Alexey A. Noyan[ab] and Kirill S. Napolskii *[bc]

Received 1st February 2022,
Accepted 14th March 2022

DOI: 10.1039/d2ma00111j

rsc.li/materials-advances

Porous anodic aluminum oxide (AAO) is a unique platform for many high-tech applications in nanotechnology, nanophotonics, and membrane science. Although scanning electron microscopy is the technique most widely used to measure the pore diameters of an AAO structure, this method accesses only a limited area of the structure and provides data with limited statistics. The AAO characteristics, averaged over the entire thickness of a porous film, can be measured by optical spectroscopy. In this paper, we demonstrate that the angular dependence of the transmittance of AAO porous films has several features caused by birefringence, which is used to measure the porosity of AAO membranes. This method of measuring porosity is accurate, precise, cheap, and does not require specific sample preparation procedures.

Introduction

Anodic aluminum oxide (AAO) films are widely applied in different fields of science and technology. They can be used as membranes,[1] templates for the preparation of nanowires[2] and nanotubes,[3] catalyst carriers,[4] substrates for gas sensors,[5] biosensors,[6] alternative energy sources,[7] and accumulators.[8] Special attention should be paid to the optical applications of AAO films, such as photonic crystals,[9,10] filters with a voltage-controlled wavelength,[11] an additional layer to increase the efficiency of the solar panels,[12] a part of the light source,[13] and templates for metamaterials based on ordered arrays of metal nanorods.[14]

Fig. 1 shows a schematic of the AAO structure. The pore diameter of an AAO is much less than the wavelength of visible light, and thus, this kind of structure may be described in terms of the effective medium model. It is worth noting that AAO has a preferential direction along the pores. All directions in the plane of the AAO film are identical, whereas the direction along the pores, which is perpendicular to the AAO plane, is distinct. The presence of this extraordinary axis may result in a birefringence effect. Birefringence has been previously observed in various nanostructures with structural anisotropy, for example, porous GaN distributed Bragg reflectors,[15] porous silicon,[16] packed films of colloidal particles,[17] and self-assembled sheets of carbon nanotubes.[18] However, birefringence in AAO is poorly studied[19,20] and is usually not considered.

The extraordinary (n_{ex}) and ordinary (n_{or}) refractive indices of AAO can be determined as follows:[19,20]

$$n_{ex}^2 = (1 - p)n_{AAO}^2 + pn_{air}^2, \quad (1)$$

$$1 - p = \frac{(n_{air}^2 - n_{or}^2)}{(n_{air}^2 - n_{AAO}^2)} \frac{n_{AAO}}{n_{or}}, \quad (2)$$

where n_{AAO} is the refractive index of the AAO cell walls, n_{air} is the refractive index of air, and p is the volume fraction of pores (porosity).

It is worth noting that the model considers AAO cell walls as a homogeneous material neglecting inner and outer layers.[21] This simplification is possible due to the low difference between the refractive indices of inner and outer layers.

For the AAO obtained in 0.3 M oxalic acid electrolyte at 5 °C and an anodization voltage of 44 V, the refractive indices, measured in reflection mode by the prism coupling technique for different polarizations of an incident beam, varied by 1.5–6%.[22] It has been experimentally proven that the birefringence effect correlates with AAO porosity. However, no quantitative theoretical explanation has been provided.

In transmission mode, the birefringence in AAO has recently been observed.[23] Although the theoretical explanation had been proven to fit the experimental data recorded at various incidence angles, the data obtained had not been applied to the calculation of some parameters of the AAO structure (such as porosity).

Scanning electron microscopy (SEM) is usually used to measure the pore diameter, interpore distance, and porosity of AAO. Although SEM can be used to easily and quickly obtain

[a] *Moscow Institute of Physics and Technology, 141700, Dolgoprudny, Russian Federation*
[b] *Department of Chemistry, Lomonosov Moscow State University, 119991, Moscow, Russian Federation*
[c] *Department of Materials Science, Lomonosov Moscow State University, 119991, Moscow, Russian Federation. E-mail: kirill@inorg.chem.msu.ru*

† Electronic supplementary information (ESI) available. See DOI: 10.1039/d2ma00111j

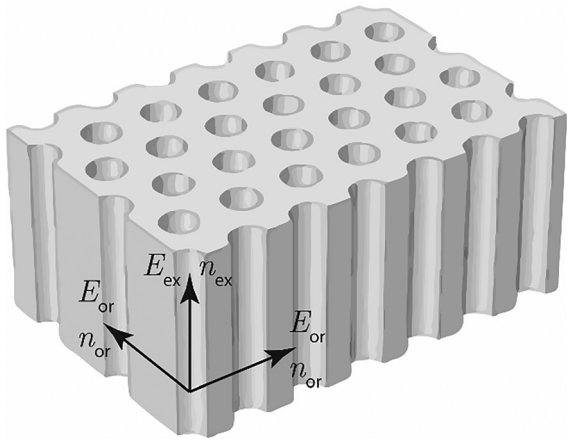

Fig. 1 A sketch of the AAO structure. Ordinary (or) and extraordinary (ex) directions are shown.

plane view and cross-sectional images, this method can access the structure only within a limited area and provides data with limited statistics. Moreover, parameters that are measured from the AAO surface do not correspond to the parameters of an average structure for the following reasons: (i) the top surface of AAO, formed at the beginning of anodization, is not identical to the structure formed later during steady-state anodization; (ii) in the cross-section, the cell walls do not crack along the diameter, and thus, only a lower-bound estimate of the pore diameter may be obtained; (iii) the bottom surface is covered with a barrier layer, which should be removed before measurements are made. To remove the barrier layer, chemical[24] or ion etching[25] procedures can be applied, however, both methods damage the AAO structure and may change the pore diameter. In some anodization regimes (*e.g.*, hard anodization under diffusion control[26] or cyclic anodization at a periodically changing voltage[27]), the porosity and channel diameter vary along the axis normal to the film. In this case, the SEM of the surface does not describe the whole structure, and measuring the average porosity may provide additional useful information.

The birefringence method to measure porosity that we present in this paper is based on transmittance measurements and therefore gives the average porosity of the sample, which is difficult to obtain with other techniques.

Experimental section

Sample preparation

Porous AAO films were obtained by anodization of a high-purity aluminum foil (99.999%) with a thickness of 500 μm. Prior to anodization, the foil was electrochemically polished to a mirror finish in a solution containing 13 M H_3PO_4 and 1.85 M CrO_3 at 80 °C as described elsewhere.[28,29] Electropolishing was carried out in impulse mode. The aluminum electrode was polarized 90 times for 3 s at an anodic current density of 0.5 A cm^{-2} with an interpulse interval of 40 s. To minimize the influence of the crystallographic orientation of the Al substrate on the parameters of AAO porous structure,[30–32] as-rolled Al foils with a fine-grained structure were used. The Al foil was anodized in 0.3 M oxalic acid (99.5%, Chimmed, Russia) at a voltage of 40 V and an electrolyte temperature of 0 °C. Two-step anodization was used. During the first anodization step, a 30 μm thick sacrificial alumina layer was formed. This layer was then selectively dissolved in an aqueous solution containing 0.5 M H_3PO_4 and 0.2 M CrO_3 at 70 °C for 30 min. The second anodization was performed under the same conditions as the first. The thickness of the AAO film was controlled coulometrically using a thickness-to-charge density ratio of 0.5 μm·cm^2 C^{-1}. The anodization was halted when the AAO thickness reached the required value in the range from 45 to 55 μm. After anodization, the porous oxide films were washed repeatedly in deionized water and dried in air.

The residual Al was dissolved in a solution of Br_2 in CH_3OH (1 : 10 vol.) at room temperature. For some of the AAO films, the barrier oxide layer was removed by chemical etching in 3 M H_3PO_4 solution at room temperature with the electrochemical detection of the pore opening moment.[33] The etching time following the pore opening moment was equal to 10 min.

To check the performance of the birefringence method in measuring porosity, a series of AAO films with various pore diameters were prepared. For this purpose, an as-prepared AAO porous film was etched in 2 M H_2SO_4 solution at 20 °C. The etching was performed in nine stages for about 20 min each. After each etching stage, the porous film was repeatedly washed in deionized water and dried before optical properties were measured.

Sample characterization

The morphology of the porous oxide films was characterized using a Carl Zeiss NVision 40 scanning electron microscope. Before SEM analysis the samples were coated with a 5 nm thick conductive layer of chromium using a Quorum Technologies Q150T ES sputter coater.

The transmittance spectra of the AAO porous films were recorded using a PerkinElmer Lambda 35 spectrophotometer. The spectra were collected at the normal incidence of light on the AAO film surface from 200 to 1100 nm with a slit width of 1 nm. A spot size at the sample position of 2×2 mm^2 was used.

The experimental setup for birefringence measurements is shown in Fig. 2. The photodiode measures the intensity of a laser beam with the wavelength $\lambda = 659 \pm 1$ nm. The AAO film was placed between two crossed or parallel polarizers and rotated around an axis perpendicular to the optical axis. The planes of polarization of the polarizers form a 45° angle with the rotation axis. The photodiode was connected to the ammeter that measured the short circuit photocurrent. The short circuit photocurrent of the Vishay BPW21R photodiode is linear over illumination; hence the current was recorded as the laser beam intensity in arbitrary units.

Theoretical section

The birefringence, Δn, is described as the difference of extraordinary (n_{ex}) and ordinary (n_{or}) refractive indices:

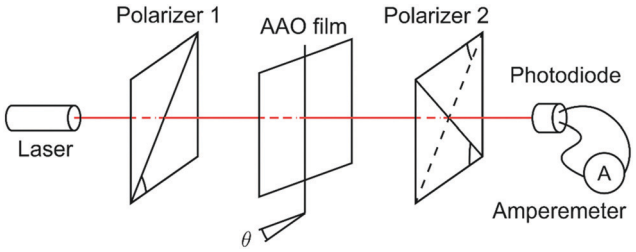

Fig. 2 Experimental setup for birefringence measurements. The photodiode measures the intensity of the laser beam. The AAO film is placed between two crossed or parallel polarizers and rotated around an axis perpendicular to the optical axis. The planes of polarization of the polarizers form a 45° angle with the rotation axis.

$$\Delta n = n_{ex} - n_{or}. \quad (3)$$

The specificity of the birefringence in AAO is that the difference, Δn, is small relative to the mean refractive index. This condition allows the simplification of the calculations.

A schematic illustration of the laser beam path through a porous AAO film is shown in Fig. 3. The mean refraction angle (β), according to Snell's law, is:

$$\sin\beta = \frac{\sin\theta}{n}, \quad (4)$$

where θ is an angle of incidence, and n is the effective refractive index of porous AAO.

In the case of birefringence, an incident beam is divided into two rays: the transverse electric (TE) mode (ray #1) with an electric field perpendicular to the plane of incidence and the transverse magnetic (TM) mode (ray #2) with an electric field in the plane of incidence. TE and TM modes of light transmit with different, but close refractive indices n_1 and n_2, respectively, and at different, but close, angles, β_1 and β_2.

$$n_1 = n_{or} \quad (5)$$

$$\frac{1}{n_2^2} = \frac{\cos^2\beta_2}{n_{or}^2} + \frac{\sin^2\beta_2}{n_{ex}^2} \quad (6)$$

As shown in Appendix 1 in the ESI,† (5) and (6) yields:

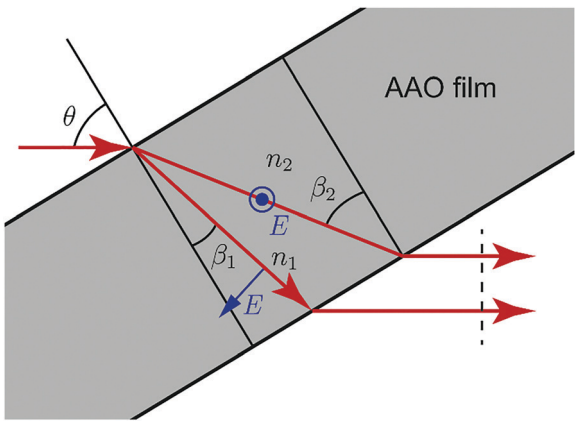

Fig. 3 Birefringence in AAO. TE and TM modes of light transmit with different effective refractive indices.

$$n_2 - n_1 = \sin^2\beta\Delta n \quad (7)$$

The TE and TM modes of light have perpendicular polarizations and may not suppress one another. However, interference is possible after the second polarizer, which projects the electric field vectors of both modes to the same axis.

The optical path difference (δ) between rays #1 and #2 determines the intensity after interference. The equation for δ is derived in Appendix 2 in the ESI:†

$$\delta = \frac{h}{\cos\beta}(n_2 - n_1), \quad (8)$$

where h is the thickness of the AAO porous film.

From (7) and (8), one can derive:

$$\delta = h\frac{\sin^2\beta}{\cos\beta}\Delta n. \quad (9)$$

The intensity after the interference of the polarized waves with phase shift $\Delta\phi = 2\pi\delta/\lambda$ is:

$$I_\perp = I_0\sin^2\left(\frac{\Delta\phi}{2}\right) = I_0\sin^2\left(\pi\frac{\delta}{\lambda}\right). \quad (10)$$

Minima are observed if the following condition is satisfied:

$$\frac{\delta}{\lambda} = m, \quad (11)$$

where m is an integer. In contrast, maxima appear at:

$$\frac{\delta}{\lambda} = m + \frac{1}{2} \quad (12)$$

In the case of parallel polarizers:

$$I_\parallel = I_0\sin^2\left(\pi\left(\frac{\delta}{\lambda} + \frac{1}{2}\right)\right). \quad (13)$$

The minima of $I_\perp$ coincide with the maxima of $I_\parallel$, and *vice versa*.

Instead of the transmittance of the membrane, the reflectance may be measured. In this case, the optical path difference δ_r will be twice δ derived for transmittance in eqn (9).

Results and discussion

In order to observe birefringence, the transmitted laser beam intensity was measured as a function of the rotation angle θ for different orientations of the polarizers. $I_\perp(\theta)$ and $I_\parallel(\theta)$ dependences recorded with crossed and parallel polarizers are shown in Fig. 4 by solid and dashed lines, respectively. As predicted by (10)–(13), the maxima of $I_\parallel(\theta)$ coincide with the minima of $I_\perp(\theta)$ and *vice versa*. When θ = 0, the optical path difference δ is 0; thus, the transmission through the system with crossed polarizers is minimal.

In raw data, the envelope of the maxima of both the $I_\perp(\theta)$ and $I_\parallel(\theta)$ curves decreases with θ. This behavior is caused by an increase in the reflectance of the AAO film with the rotation angle. To compensate for this effect, the intensity ($I_\perp$ or $I_\parallel$), measured after the polarizer 2 (Fig. 2), was normalized to the intensity of the laser beam passed through the polarizer 1 and the sample ($I_{p1}(\theta)$). In the absence of the second polarizer, no

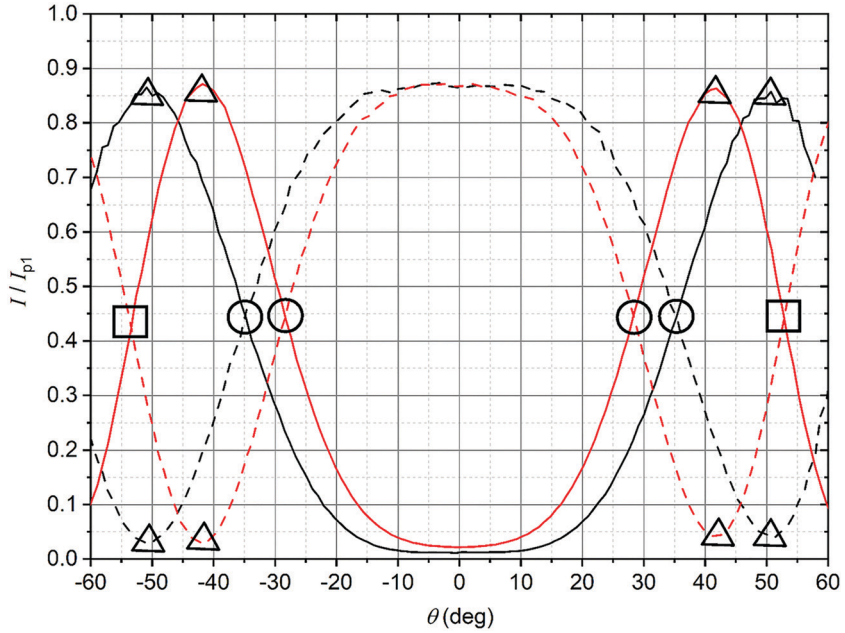

Fig. 4 The dependence of the intensity of the transmitted laser beam on the rotation angle of an AAO film placed between two polarizers whose vibration directions are oriented perpendicular (solid lines) and parallel (dash lines) to each other. Specific points corresponding to various values of δ/λ are shown: 0.25 (circles), 0.5 (triangles), and 0.75 (squares). Data are presented for the as-prepared AAO film (black lines) and the AAO film after barrier layer etching (red lines).

interference of polarized waves occurs, and $I_{p1}(\theta)$ is monotonous without maxima or minima.

Specific points (extrema or the points of intersection) corresponding to δ/λ of 0.25, 0.5, and 0.75 are indicated in Fig. 4 by circles, triangles, and squares, respectively. The θ positions of these points were used to calculate β using (4), taking into account the effective refractive index (n) of the films (Appendix 3 in the ESI†). Then, the birefringence, $\Delta n/n$, was found according to (9), using the thickness of the AAO film, h = 52.5 ± 0.5 μm, determined from the cross-sectional SEM images. The results are listed in Table 1.

The values of $\Delta n/n$ obtained were used to refine n_{AAO} and calculate the porosity (p) by an iteration algorithm described below. The dependence of $\Delta n/n = 2(n_{ex} - n_{ox})/(n_{ex} + n_{ox})$ on the porosity of the AAO film is shown in Fig. 5. The ordinary and extraordinary refractive indices were calculated by (1) and (2), using n_{air} = 1.00. As the starting point, the refractive index of the AAO cell walls, n_{AAO}, was taken as equal to 1.765 (the refractive index of corundum at 660 nm[34]). The following iteration algorithm was used (i is the iteration step number):

1. The dependence of $\Delta n/n$ on the porosity (p) was calculated using n_{AAO_i}.

Table 1 Birefringence in porous anodic aluminum oxide films

	δ/λ	θ, °	β, °	$\Delta n/n$	p, %
As-prepared AAO film	0.25	35.1	20.9	0.0147	10.1
	0.5	50.8	28.7	0.0152	10.4
AAO film after barrier layer etching	0.25	28.3	17.5	0.0210	14.7
	0.5	41.6	24.9	0.0204	14.2
	0.75	53.1	30.5	0.0200	14.0

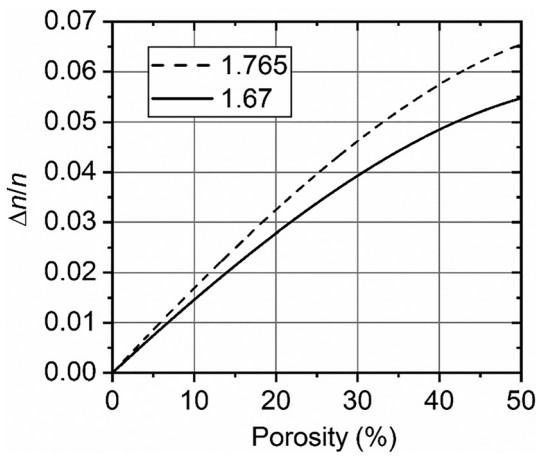

Fig. 5 Dependence of the birefringence on the porosity of the AAO film. Data calculated for two values of n_{AAO} are shown: 1.765 (dashed line) and 1.67 (solid line).

2. The porosity p_{i+1} was determined from the $p\left(\frac{\Delta n}{n}\right)$ graph.

3. $n_{AAO_{i+1}}$ was calculated by substituting p_{i+1} into (2)

4. Steps #1–3 were repeated until the changes in n_{AAO} and p became lower than 1%.

After three iterations, the refined value n_{AAO} = 1.67 was obtained. This value is in good agreement with the refractive indices of amorphous Al_2O_3 films formed using different methods: reactive sputtering ($n_{Al_2O_3}$ = 1.63[35]), electron beam evaporation ($n_{Al_2O_3}$ = 1.60–1.71[36]), and spray pyrolysis ($n_{Al_2O_3}$ = 1.58[36]). The close value of the refractive index of the AAO cell walls (n_{AAO} = 1.64) was obtained for porous films

formed in selenic acid electrolyte.[37] A substantially lower value n_{AAO} = 1.55 was found for the AAO film prepared in 0.3 M oxalic acid electrolyte at 40 V.[38] However, in this case, the geometrical parameters were measured with low accuracy based on SEM data. The calculated values of AAO porosity for the case of n_{AAO} = 1.67 are listed in Table 1.

It is worth noting that knowledge of the intrinsic value of n_{AAO} is not critically important in the birefringence method for measuring porosity described in this work. If n_{AAO} differs from 1.67 by 2%, the error in $\Delta n/n$ is 5.5%, which results in a relative error of 5.5% in the porosity. In comparison, if porosity is determined from eqn (1) with known n and n_{AAO}, a 2% error in n_{AAO} results in a relative error of 36% in the porosity.

The shifts of the curves in Fig. 4 for as-prepared and etched AAO films are well-defined, allowing the detection of the increase in porosity during the barrier layer etching with high precision. According to birefringence measurements, the porosity increased from 10.3% to 14.3%.

In order to show that the $I_{\perp}(\theta)$ and $I_{\parallel}(\theta)$ curves correspond to the functions (10) and (13) over a wide range of θ, the δ/λ ratio was calculated for each angle from the experimental data (Fig. 4). (10) and (13) as the backward equations for δ/λ have an infinite number of solutions. The correct solution was selected for each angle, taking into account that the function $\frac{\delta}{\lambda}(\theta)$ is monotonous, continuous, and $\frac{\delta}{\lambda}(0) = 0$. From these assumptions, a single solution for each angle exists. For instance, for the AAO film after barrier layer etching $\frac{\delta}{\lambda}(\theta)$ dependence can be given as the following piece-wise function:

$\frac{\delta}{\lambda} = \frac{1}{\pi}\mathrm{asin}\left(\sqrt{\frac{I}{I_0}}\right)$ at θ from -41.6° to 41.6° (41.6° angle corresponds to δ/λ = 0.5);

$\frac{\delta}{\lambda} = 1 - \frac{1}{\pi}\mathrm{asin}\left(\sqrt{\frac{I}{I_0}}\right)$ at θ from -60° to -41.6° and from 41.6° to 60°.

According to (9), $\frac{\delta}{\lambda}(\theta)$ should be linearized in coordinates $\left(\frac{\delta}{\lambda}; \frac{\sin^2\beta}{\cos\beta}\right)$ with the slope $\frac{hn}{\lambda}\frac{\Delta n}{n}$. The experimentally observed dependence of δ/λ on $\frac{\sin^2\beta}{\cos\beta}$ is shown in Fig. 6 by scatters. As the data (Fig. 4) do not perfectly fit the 0–1 range, they were dragged as shown in Appendix 4 in the ESI,† to avoid function jumps. The experimental data presented in Fig. 6 fit perfectly to linear functions, which confirmed that the theory and the experiment were consistent. The values calculated from the slopes are listed in Table 2. The calculated porosity of both the as-prepared AAO film and the membrane after barrier layer etching agrees with the values in Table 1.

Linearization of the dependence of δ/λ on $\frac{\sin^2\beta}{\cos\beta}$ does not improve the accuracy of the porosity calculation but has an advantage in determining the porosity of thin films when points corresponding to the specific values of δ/λ may not be observed. In particular, for a membrane with porosity of 10%,

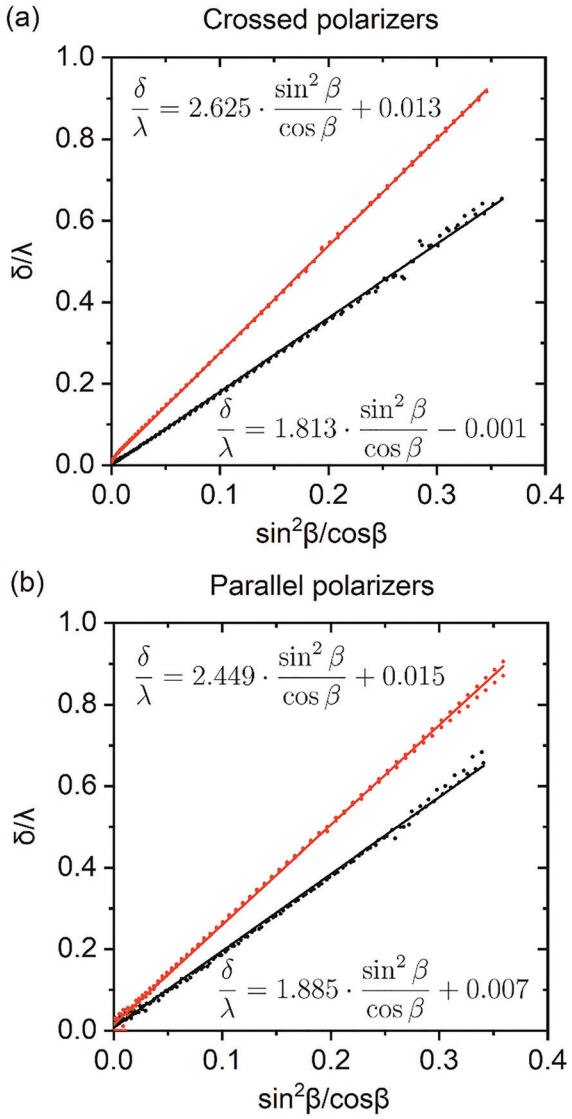

Fig. 6 The optical path difference divided by the wavelength of incident beam as a function of $\frac{\sin^2\beta}{\cos\beta}$. Data for AAO films placed between two polarizers whose vibration directions are oriented perpendicular (a) and parallel (b) to each other are shown. Black curves correspond to the as-prepared AAO films, whereas red curves are for the membranes after barrier layer etching.

the intersection of angular dependencies of $I_{\perp}$ and $I_{\parallel}$ can be observed only for the samples thicker than 15 μm.

To check the performance of the birefringence method in measuring porosity over a wide range, a series of AAO films etched in 2 M H_2SO_4 solution at 20 °C for up to 3 hours was prepared. The experimental dependences of $I_{\perp}/I_{p1}$ and $I_{\parallel}/I_{p1}$ on the rotation angle of the AAO film are shown in Appendix 5 in the ESI.† The angular dependence was used for the calculation of the mean porosity of the films under study. Then, an average pore diameter (D_p) was calculated using the equation:

$$D_p = \sqrt{\frac{4p}{\pi\rho_S}} \quad (14)$$

Table 2 Birefringence and porosity values, calculated from the linearization of the $\frac{\delta}{\lambda}\left(\frac{\sin^2\beta}{\cos\beta}\right)$ function

	Measurement geometry	Slope	$\Delta n/n$	p,%
As-prepared AAO film	Crossed polarizers	1.81	0.0141	9.6
	Parallel polarizers	1.88	0.0146	10.0
AAO film after barrier layer etching	Crossed polarizers	2.63	0.0210	14.7
	Parallel polarizers	2.45	0.0195	13.6

where ρ_S = 113 μm^{-2} is the number of pores per unit area, determined from the SEM data (Fig. 7). The evolution of D_p with the etching duration is shown in Fig. 8. The pore diameter was found to increase linearly with time. The error in D_p may be estimated as 0.3 nm from the deviation of points. Therefore, the obtained data demonstrate the high sensitivity of the presented method.

According to SEM, the porosity of the as-prepared film is 10 ± 1% (D_p = 33.5 ± 1.6 nm), whereas the porosity of the etched for 3 h film is 18 ± 1% (D_p = 45.0 ± 1.2 nm). Hence, SEM data are in agreement with birefringence measurements (Fig. 8). However, these methods allow different film parameters to be obtained: the mean porosity of the whole membrane is measured with the birefringence method, and only the film surface is observed on SEM.

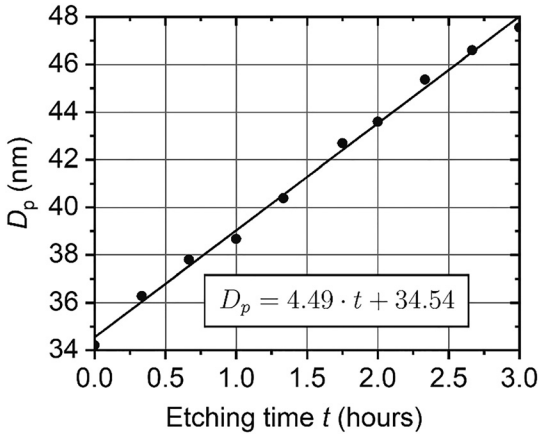

Fig. 8 Dependence of an average pore diameter on the etching duration in 2 M H_2SO_4 solution at 20 °C.

Conclusions

In summary, the transmittance of a laser beam through a porous AAO film placed between two polarizers was studied both theoretically and experimentally. The birefringence caused by the anisotropy of the AAO structure manifests itself as a transmittance oscillation with the angle of incidence. The experimentally observed dependencies are in good agreement with theoretical equations.

Specificity of the birefringence in AAO is that the difference between extraordinary and ordinary refractive indices, Δn, is small in relation to the mean effective refractive index, n. For the series of AAO films obtained in 0.3 M oxalic acid electrolyte at 40 V and electrolyte temperature of 0 °C, $\Delta n/n$ varied from 0.014 to 0.028. The birefringence $\Delta n/n$ increases with the rise of porosity.

The birefringence effect in AAO was applied to calculate the refractive index of the AAO cell walls and film porosity for the first time. Only the AAO film thickness and the effective refractive index, which can be obtained easily by SEM measurements and analysis of Fabry–Pérot oscillations, are needed to measure these parameters.

The high sensitivity of the birefringence effect to the AAO porosity was proved experimentally. Even after barrier layer dissolution with electrochemical detection of the pore opening moment, an increase in the AAO porosity was unambiguously detected. A constant etching rate was observed in a series of AAO porous films etched in 2 M H_2SO_4 solution at 20 °C.

It is worth noting that eqn (1) and (2) were derived without assumptions on the 2D hexagonal ordering of the pores, and, thus, the measurements are not affected by the domain boundaries and other defects of porous structure. High accuracy, precision, low cost, and an easy sample preparation procedure make the method developed in this work an effective tool to measure the porosity of AAO films. The absence of quantitative

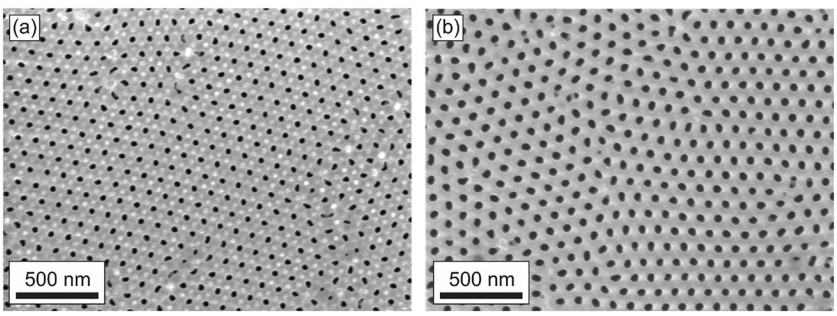

Fig. 7 SEM image of the as-prepared AAO porous film (a) and the same film after etching in 2 M H_2SO_4 solution at 20 °C for 3 hours (b). The top surfaces of the films were measured.

approaches to solve this task using other techniques will guarantee worldwide interest in the method from scientists working in various areas of nanotechnology, membrane science, and other fields that we cannot yet envision. The suggested approach can be applied to measure the porosity of other optically transparent materials, containing aligned cylindrical channels, such as anodic titanium oxide, porous silicon and silicon oxide, track-etched membranes, and porous films based on diblock copolymers. Another promising application of the birefringence method is mapping of AAO to study the spatial distribution of non-homogeneity and anisotropy of its structure. In this case, a laser beam spot size much smaller than the lateral size of Al grains or AAO domains should be provided.

Conflicts of interest

There are no conflicts to declare.

Acknowledgements

A. A. N. thanks the financial support from the Russian Foundation for Basic Research (grant no. 20-33-90084). The evaluation of the performance of the developed method for the analysis of anodic aluminum oxide films with a wide range of porosity was supported by the Russian Science Foundation (grant no. 18-73-10151).

References

1 X. Shi, A. Xiao, C. Zhang and Y. Wang, *J. Membr. Sci.*, 2019, **576**, 116.
2 C. Wang, L. Zheng, R. Chang, L. Du, C. Zhu, D. Geng and D. Yang, *ACS Appl. Mater. Interfaces*, 2018, **10**, 29965.
3 Q. Xu, G. Meng and F. Han, *Prog. Mater. Sci.*, 2018, **95**, 243.
4 N. Qiao, Y. Nong, N. Liu and Y. Liang, *Mater. Chem. Phys.*, 2019, **225**, 458.
5 N. John, P. Thomas, K. V. Divya and K. E. Abraham, *Nanotechnology*, 2019, **29**, 335503.
6 Z. Li, C. Liu, V. Sarpong and Z. Gu, *Biosens. Bioelectron.*, 2019, **126**, 632.
7 W. Xin, Z. Zhang, X. Huang, Y. Hu, T. Zhou, C. Zhu, X. Kong, L. Jiang and L. Wen, *Nat. Commun.*, 2019, **10**, 3876.
8 Q. Wei, Y. Fu, G. Zhang, D. Yang, G. Meng and S. Sun, *Nano Energy*, 2019, **55**, 234.
9 H. Wang, Z. Yin, W. Xu, D. Zhou, S. Cui, X. Chen, H. Cuib and H. Song, *Nanoscale*, 2016, **8**, 10004.
10 K. S. Napolskii, A. A. Noyan and S. E. Kushnir, *Opt. Mater.*, 2020, **109**, 110317.
11 P. Lo, G. Luo, C. Lee and W. Fang, *J. Micromech. Microeng.*, 2015, **25**, 025001.
12 L. Wu, H. Zhang, F. Qin, X. Bai, Z. Ji and D. Huang, *Opt. Commun.*, 2017, **385**, 205.
13 C. H. Lin, C. Y. Kang, T. Z. Wu, C. L. Tsai, C. W. Sher, X. Guan, P. T. Lee, T. Wu, C. H. Ho, H. C. Kuo and J. H. He, *Adv. Funct. Mater.*, 2020, **30**, 1909275.
14 P. R. Evans, R. Kullock, W. Hendren, R. Atkinson, R. J. Pollard and L. M. Eng, *Adv. Funct. Mater.*, 2008, **18**, 1075.
15 P. H. Griffin, K. M. Patel, T. Zhu, R. M. Langford, V. S. Kamboj, D. A. Ritchie and R. A. Oliver, *J. Appl. Phys.*, 2020, **127**, 193101.
16 D. Kovalev, G. Polisski, J. Diener, H. Heckler, N. Künzner, V. Y. Timoshenko and F. Koch, *Appl. Phys. Lett.*, 2001, **78**, 916.
17 K. Inoue and S. Inasawa, *RSC Adv.*, 2020, **10**, 2566.
18 R. Duggal, F. Hussain and M. Pasquali, *Adv. Mater.*, 2006, **18**, 29.
19 E. S. Kooij, A. C. Galca, H. Wormeester and B. Poelsema, in *Dekker Encyclopedia of Nanoscience and Nanotechnology*, ed. J. A. Schwarz, S. E. Lyshevski and C. I. Contescu, CRC Press, USA, 3rd edn, 2004, pp. 3685–3695.
20 E. S. Kooij, H. Wormeester, A. C. Galca and B. Poelsema, *Electrochem. Solid-State Lett.*, 2003, **6**, 52.
21 G. D. Sulka, in *Nanostructured Materials in Electrochemistry*, ed. A. Eftekhari, Wiley-VCH, Germany, 2008, pp. 1–116.
22 S. H. Gong, A. Stolz, G. H. Myeong, E. Dogheche, A. Gokarna, S. W. Ryu, D. Decoster and Y. H. Cho, *Opt. Lett.*, 2011, **36**, 4272.
23 C. Wang, P. Qin, D. Lv, J. Wan, S. Sun and H. Ma, *Opt. Express*, 2020, **28**, 6740.
24 C. Y. Han, G. A. Willing, Z. Xiao and H. H. Wang, *Langmuir*, 2007, **23**, 1564.
25 W. Lee, R. Ji, U. Gosele and K. Nielsch, *Nat. Mater.*, 2006, **5**, 741.
26 V. Vega, J. García, J. M. Montero-Moreno, B. Hernando, J. Bachmann, V. M. Prida and K. Nielsch, *ACS Appl. Mater. Interfaces*, 2015, **7**, 28682.
27 S. E. Kushnir, T. Yu Komarova and K. S. Napolskii, *J. Mater. Chem. C*, 2020, **8**, 3991.
28 A. Mozalev, S. Magaino and H. Imai, *Electrochim. Acta*, 2001, **46**, 2825.
29 I. V. Roslyakov, E. O. Gordeeva and K. S. Napolskii, *Electrochim. Acta*, 2017, **241**, 362.
30 L. Sacco, I. Florea, M. Châtelet and C. S. Cojocaru, *Thin Solid Films*, 2018, **660**, 213.
31 I. V. Roslyakov, A. P. Chumakov, A. A. Eliseev, A. P. Leontiev, O. V. Konovalov and K. S. Napolskii, *J. Phys. Chem. C*, 2021, **125**, 9287.
32 I. V. Roslyakov, D. S. Koshkodaev, A. A. Eliseev, D. Hermida-Merino, V. K. Ivanov, A. V. Petukhov and K. S. Napolskii, *J. Phys. Chem. C*, 2017, **121**, 27511.
33 M. Lillo and D. Losic, *J. Membr. Sci.*, 2009, **327**, 11.
34 I. H. Malitson, *J. Opt. Soc. Am.*, 1962, **52**, 1377.
35 J. Kischkat, S. Peters, B. Gruska, M. Semtsiv, M. Chashnikova, M. Klinkmüller, O. Fedosenko, S. Machulik, A. Aleksandrova, G. Monastyrskyi, Y. Flores and W. Ted Masselink, *Appl. Opt.*, 2012, **51**, 6789.
36 K. S. Shamala, L. C. S. Murthy and K. N. Rao, *Mater. Sci. Eng., B*, 2004, **106**, 269.
37 A. I. Sadykov, S. E. Kushnir, I. V. Roslyakov, A. E. Baranchikov and K. S. Napolskii, *Electrochem. Commun.*, 2019, **100**, 104.
38 A. Hierro-Rodriguez, P. Rocha-Rodrigues, F. Valdés-Bango, J. M. Alameda, P. A. S. Jorge, J. L. Santos, J. P. Araujo, J. M. Teixeira and A. Guerreiro, *J. Phys. D: Appl. Phys.*, 2015, **48**, 455105.